Thermal Regulation in Multiple-Source Arc Welding Involving Material Transformations

An analytic model can be used as a basis for in-process control of welding temperature

BY C. C. DOUMANIDIS

ABSTRACT. This article addresses regulation of the thermal field generated during arc welding, as the cause of solidification, heat-affected zone and cooling rate related metallurgical transformations affecting the final microstructure and mechanical properties of various welded materials. This temperature field is described by a dynamic real-time process model, consisting of an analytical composite conduction expression for the solid region, and a lumped-state, double-stream circulation model in the weld pool, integrated with a Gaussian heat input and calibrated experimentally through butt joint GMAW tests on plain steel plates. This model serves as the basis of an in-process thermal control system employing feedback of part surface temperatures measured by infrared pyrometry, and real-time identification of the model parameters with a multivariable adaptive control strategy. Multiple heat inputs and continuous power distributions are implemented by a single time-multiplexed torch, scanning the weld surface to ensure independent, decoupled control of several thermal characteristics. Their regulation is experimentally obtained in longitudinal GTAW of stainless steel pipes, despite the presence of several geometrical, thermal and process condition disturbances of arc welding.

Introduction

Since the first historical reference to forge welding of the Greek hero Achilleus's armor by the smith of the Olympian gods, Hephaistos, in the *Iliad of Homer* (11th century BC, Ref. 1), the welding literature has witnessed several important developments and improvements in the mechanical properties of the weld joints. In arc welding, most research efforts have primarily addressed the importance of the weld bead geometry on the useful cross-sectional area and thus the loading capacity of the joint (Refs. 2, 3). A second quality attribute of the weld, its residual stress and distortion state, has been related to stress concentration at critical points of the weld morphology (reinforcement and root undercuts, ripples, craters, cracks) that may lead to fracture under low applied load, or deformation instabilities such as buckling (Ref. 4). Last, the weld microstructure has been studied in connection to the local material properties and the homogeneity and isotropy of their distribution, as well as the presence of phases and structures providing initiation sites for brittle or ductile fracture, fatigue fracture, stress corrosion cracking, etc. (Refs. 5, 6). These failure modes are particularly crucial for welds, since the propagation of a crack across a weld bead cannot be arrested as conveniently as in a riveted or bonded joint.

C. C. DOUMANIDIS is an Assistant Professor in the Thermal Analysis for Materials Processing Laboratory, Tufts University, Medford, Mass.

KEY WORDS

Material Transform.
Multisource Arc Weld
Thermal Field
Multitorch Control
Process Model
Transv. Torch Osc.
Control Design
Welding Controls
Multiple Heat Inputs
Power Distributions

Regarding this final weld structure and material properties, the metallurgical transformations taking place during the process, and the resulting distribution of material phases can be generally classified as follows:

1) *Solidification Structures and Defects.* These are developed upon local cooling of the molten material below the solidus isotherm Tm, *i.e.*, upon crossing the solidification front of the weld pool. Microgeometrical defects consist of porosity, inclusions, unfused areas and shrinkage cracks, while microstructural faults include columnar dendritic structures, nonuniform grain size, segregated areas and undesirable phases in the weld bead. Composition and structure changes because of dilution of the base metal with filler metal may also occur in welding with a consumable electrode (e.g., gas metal arc welding, GMAW) (Ref. 7).

2) *Equilibrium Structures in the Heat-Affected Zone (HAZ).* These thermodynamically stable structures are developed by metallurgical transformations in certain materials, as they are cooled below a HAZ isotherm temperature T_h. They form mechanically weak recovery, recrystallization or coarse-grain zones, as well as areas of undesirable phases, such as the overaging zone of precipitation-hardened aluminum alloys, or even regions contaminated from the welding environment or the diluted pool. In all cases, the nucleation of equilibrium structures R (in kg) is thermally activated and described by Arrhenius's equation (Ref. 5):

$$R(t)=\int_0^t r.exp\left(-\frac{Q}{kT(\tau)}\right)d\tau$$

where r is a transformation rate factor (in kg/s), Q is the activation energy per particle (J), k the Boltzmann constan, τ is a

Table 1 — Thermal Microstructural Transformations Observed in Various Welded Materials

Material	Weld Bead	Heat-Affected Zone	Cooling Rate
Low-carbon steels (mild): C<0.25%	General solidification defects	Grain growth, low ductility	Occasional hard bainite, microsegreg, integran. martensite, fine pearlite
Medium-carbon steels (C:0.25–0.50%	Solidification defects, dilution of melt	Grain growth, recrystallization	Martensite formation
High-carbon steels C>0.5%	Solidification defects, H-embrittlement	Recrystallization, recovery	Martensite formation
Free-machining steels S>0.05%, P>0.04%	Porosity from H_2S entrapment	Embrittlement from hot shortness	Occasional martensite
Low-alloy steels Mo + Cr + Ni + Mn + Si + Cu + T + V + Cb<3%	Dissolved gases, dilution of melt	Sensitization, hot shortness (esp. annealed, w. Cu, S)	Martensite formation
Medium-alloy steels all. elements 3–10%	Solid. defects, dilution el. oxidation, moisture	Sensitization, grain growth, hot shortness	Martensite formation
Mart. stainless steels Cr < 16%, C:0.35–0.6%	As above, H-embrittlement	Dominant sensitization	Martensite, brittle inter. nets, thermal cracking
Ferritic stainless steels Cr > 16%, C:0.12–0.2%	Columnar structure, dilution, oxidation	Sensitization, grain growth, σ-phase	Thermal cracks, 470°C embr, C-supersaturation
Austenitic stainless st. Cr > 12%, Ni, low C	As above	Domin. sensitization, σ-phase formation	Thermal cracks, C-supersaturation, δ-ferrite
Austenitic Hadfield st. Mn: 10–14%, Ni, C: 0.75–1.50%	Dilution in the melt, oxidation from air	Austen. grain growth transient martensite	Cracking, pearlite w/Ni, transient martensite at 260°C
Nickel & alloys Monel (Cu), Inconel (Cr), Hastelloys (Mo)	Gas porosity, dilution in the pool	Inconel sensitization, sulfidation at 650°C	Pronounced thermal cracking
Copper (tough pitch, O-free, P-deoxidized)	Dendrites, gas pores, dilution esp. w. Ag, Sn	Grain growth, oxidation, hot shortness	Cracking tendency
Brasses (red 5c–20% Zn, yellow 20–45% Zn, Pb)	As above	Grain growth, hot short, volatilization	Cracking tendency, esp. of hot short brasses
Bronzes (Si: 1–4%, P: 0.1–0.35%, Sn:3.5–11% Ni:10–30%, Al:5–10%)	Dendritic structure (except Al-bronzes), oxidation from air	Hot shortness (ex. Al) grain growth	Cracking of hot short bronzes, surface undercuts of Al-bronzes
Aluminum & alloys w. Mn, Mg (series 1,3,5)	Dilution in the pool, oxidation effects	Grain growth of Al & annealed alloys	Occasional cracking tendency
Age-hardened H.S. Al alloys (series 2, 4, 6, 7)	As above	Overaging of Θ-phase, corrosion cracking	As above
Magnesium & alloys w. Al, Mn, Zn	Dilution in the pool, oxidation from air	Grain growth, stress corrosion cracking	Cracking w. hot shortness; formation of α-phase
Titanium & alloys α: pure, w. Al, O, N, C; β: w. Fe, Cr, Mo, Mn, V, Sn; $\alpha + \beta$	Brittle intermetallics, solution strengthening freezing segregation	Oxidation, grain growth of α-phase, contamination and reactivity at 650°C,	Grain size of α-β phase, dispersion-coherency & hardening, stabilization of β, noneq. brittle str.

dummy time integration variable, and T the time-dependent local temperature of the material (K).

3) *Nonequilibrium Structures Related to the Cooling Rate* $T_{cr} = \partial T/\partial t$. These are generated by kinetically favored transformations upon rapid cooling below a critical temperature T_c. Classical examples include the martensitic transformation of hardenable steels and the thermal cracking or structural embrittlement zones of highly alloyed steels and hot short metals. The condition for the formation of such nonequilibrium structures,

$$T(t) = \int_0^t T_{cr}(\tau)d\tau \leq T_c(t)$$

is based on a critical temperature transient $T_c(t)$ of the continuous time-transformation (CTT) diagram of the welded material (Ref. 5).

Table 1 illustrates these three types of microstructural transformations and the associated weld deficiencies for a wide range of common welded metals. The importance of their influence on the mechanical properties of the joints is best demonstrated by the volume of related welding research, which addresses off-line control of the material structure. In industrial practice, though, real-time control of the weld microstructure during the process is required to cope with variable or uncertain welding conditions (disturbances), such as the arc efficiency, and to eliminate costly overdesign of the joint, nondestructive material testing and remedial postprocessing procedures, such as remelting, postheating, vibratory stress relieving, etc. However, the development of such in-process feedback controllers, that would detect the weld microstructure and modify the process conditions to regulate the weld material properties, is hindered by the unavailability of specialized real-time structure sensors and dynamic models, on which the controller design must be based. Moreover, additional difficulties for feedback control are introduced by the large time delays between these transient features during the process and the final ones in the weld joint.

As a result, the few research efforts in this direction have focused on regulation of a few distinct microstructural characteristics, such as the HAZ width or the centerline cooling rate (Refs. 8–10). For example, Ref. 9 presents an ad hoc empirical model of GMAW on mild steel plates and attempts to control HAZ and cooling rate related temperatures by modulating a longitudinal reciprocation of the torch. However, this thermal control design is dedicated to a specific welding process, part geometry and material and torch motion pattern, and thus is of limited applicability.

The objective of this study is to establish a general and systematic methodology for simultaneous feedback control of several thermal features in various arc welding configurations, which determine the quality characteristics of the material structure of the joint. Since all three types of such features were shown to depend deterministically on the transient temperature field developed during welding, real-time dynamic thermal modeling and noncontact infrared sensing will be designed for this purpose. Finally, a multiple heat source arrangement will be introduced to decouple the regulation of the material microstructure and properties. In this configuration, multiple localized heat inputs are implemented by a single time-multiplexed torch, which is rapidly guided periodically to the respective weld positions, while its power is adjusted so as to provide the desired concentrated heating effects. Although a preset transverse oscillation of the heat source (weaving) has been commonly practiced in automated arc welding, in-process control of the motion and power of the torch by infrared temperature feedback will be demonstrated as the basis for thermal regulation during welding.

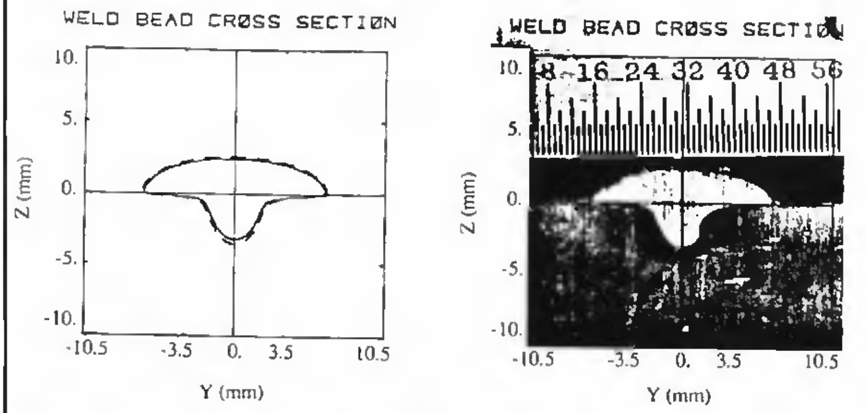

Fig. 1 — Weld bead cross-section for experimental calibration of the model (- - - : calibrated model; ____ : recalibrated model).

Thermal Modeling of Weld Structure

In the welding bibliography, temperature field models may be distinguished to: 1) provide physical insights, but with assumptions limiting their applicability (analytical models); 2) ensure flexibility of conditions, at the expense of computational efficiency (numerical models); and 3) fit well static experimental data at rather narrow process condition ranges (empirical models).

The intended use of a thermal model as a design basis for microstructure control requires a dynamic process description, executable at real-time speed, with good flexibility in the welding conditions. Table 2 summarizes most representative research efforts in the direction of analytical thermal weld modeling (Refs. 11–29). It can be clearly seen that no single existing analytical model is based on assumptions applying to all industrial arc welding situations. Thus, a new comprehensive thermal model is devised below, to combine the dynamic insight of analytical modeling to the flexibility of numerical simulation, and the experimental fidelity of empirical expressions. This mixed model consists of separate but integrated descriptions of the solid region, governed by composite conduction from an ideal source pair,

Table 2 — Analytical Thermal Models in the Welding Literature

Researcher	Ref.	Year	Geometry of joint & source	Materials	Heat Transfer	Special Conditions
Roberts	11	1923	2D pl/line srce	homogen-isotropic	diffusion eq.	gen. diffusion
Rosenthal Rykalin	12/13 14	1941 1951	2D, 3D, 2.5D point & line src	no temp. variation no phase transform	conduction no heat losses	limited exper. verification
Wells	15	1952	2D pl/line srce consumable el.	same as above	conduction matl. deposition	isotherm width, gap. filling, ripple
Roberts	16	1954	2D-finite plate	same as above	same as above	num. verification cooling rate
Grosh Trabant	17	1956	1D, 2D, 3D concentrated sr.	linear temp. depend. no latent effects	negligible heat losses	experimental verification
Carslaw Jaeger	18	1959	2D, 3D, strips point/line/plane	no temp. variation latent heat effects	heat losses by convection	classical conduction monograph
Adams Jhaveri	19 20	1958 1962	2D, 3D, 2.5D plates	no temp. variation	surf. convection & radiation	peak T, cooling rate, centerline T
Barry	21	1963	2D, 3D, 2.5D	average temp. dep.	dim. anal. charts	average T, n
Myers	22	1967	2D, 3D, 2.5D 1D (electrode)	no temp. variation	conduction + surf. convection	peak T, cool. rates isotherms, T-prof.
Kazimirov	23	1973	2D plate	temp. dependence constant α	conduction + surf. convecton	experimental verification
Kopersak	24	1973	3D pool geom.	$c_p$solid = $c_p$liquid latent heat effects	conduction in the melt	average pool temperatures
Malmuth	25	1974	3D GTAW	latent heat of fusion	var. efficiency cond. to fixtures	pool size, IR pyr. dry calorim. for n
Nedoseka	26	1977	2.5 D plate	temp. dependence	convection & radiation losses	volumetric T distribution
Nunes	27	1983	mainly 2D	to temp. variation	phase changes pool circulation	dipoles, quadrpls empir. calibration
Willgoss	28	1984	spray GMAW electrode (1D)	Al & mild steel latent heat effects	thermal equil. Joule heating	find I, f, stickout from V, R, length
Tsai	29	1988	Gaussian sourc.	no temp. variation	conduction	calibration of n, σ

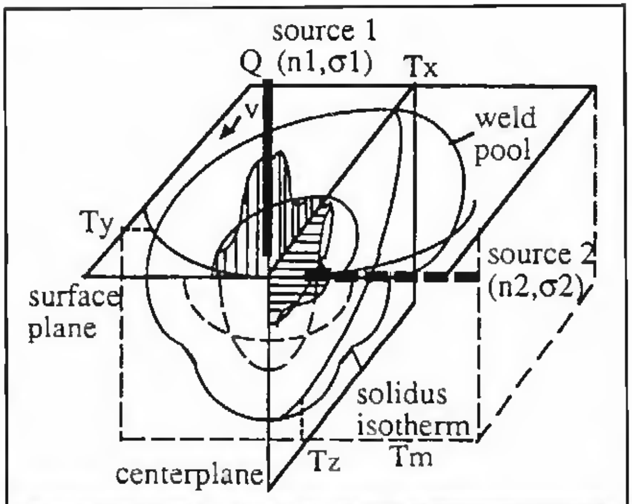

Fig. 2 — Thermal conduction field from a Gaussian source pair.

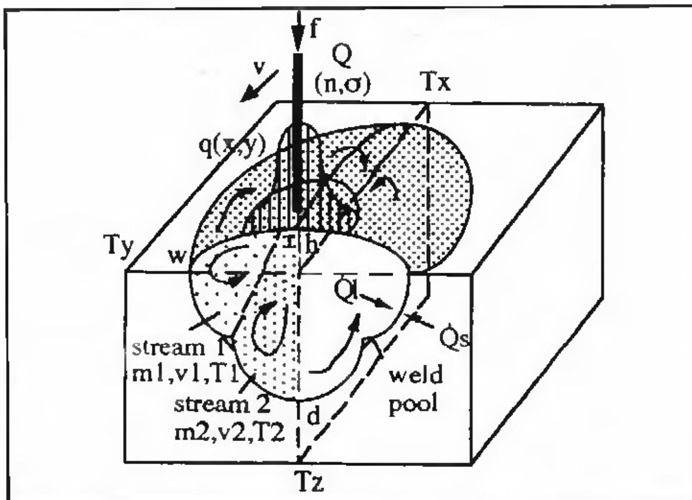

Fig. 3 — Double-stream circulation pattern in the weld pool.

and the weld pool, characterized by lumped state balances of a double-stream circulation pattern.

Solid Area

The temperature field developed through isotropic thermal conduction in the solid region by a Gaussian heat source, including concentrated point, line, surface and spatial power distributions from the arc in all analytical models of Table 2, yields isotherms of ellipsoidal cross-section. Thus, to obtain the familiar, general dished-in weld pool profile (T_m isotherm), with the lateral extensions and penetration finger as in the GMAW weld of Fig. 1, the combination of two such elliptical fields, generated by a pair of hypothetical Gaussian heat distributions on the weld surface and the centerplane of Fig. 2, is proposed in this model. The centerplane component of this heat source pair describes the arc heat transfer in the depth direction, through the deceleration of energy carriers (electrons, ions, etc.), possible electromagnetic stirring, Joule heating, etc. The power densities of the source pair for a torch power Q in the (x,y,z) coordinate system are characterized by the partial efficiencies and distribution radii (n_1,σ_1) and (n_2,σ_2) as follows (Ref. 30):

$$q_1(x,y)=\frac{n_1Q}{2\pi\sigma_1^2}\ exp\left(-\frac{x^2+y^2}{2\sigma_1^2}\right)$$
$$q_2(x,z)=\frac{n_2Q}{2\pi\sigma_2^2}\ \exp\left(-\frac{x^2+z^2}{2\sigma_2^2}\right) \qquad (1)$$

By proper adjustment of the source pair parameters (n_i,σ_i), a variety of realistic isotherm and weld bead cross-section shapes can be generated by the composite temperature field, which, for temperature-independent material properties, results from the linear superposition of the respective fields for each source component — Fig. 2. For symmetric butt joint welding of insulated plates of finite thickness, an expression for the composite temperature field is derived by the method of images (Ref. 18):

$$T(x,y,z;t)=T_0+\sum_{k=-\infty}^{\infty}\left[\begin{array}{l}T(x,y,z+2kD;n_1,\sigma_1,t)+\\ T(x,z,+2kD,y;n_2,\sigma_2,t)\end{array}\right]$$

where

$$T(x,y,z;n,\sigma,t)=\int_0^t\frac{nQ}{\pi\rho c}\cdot\frac{(4\pi\alpha\tau)^{-\frac{1}{2}}}{2\alpha\tau+\sigma^2}\cdot exp\left(-\frac{(x+v\tau)^2+y^2}{4\alpha\tau+2\sigma^2}-\frac{z^2}{4\alpha\tau}\right)dt \qquad (2)$$

where T_0 is the preheat temperature, D the plate thickness, Q and v the torch-power and velocity, n and σ the pair efficiency and distribution radius, ρ, c and α the material density, heat capacity and thermal diffusivity. This calculation needs to be performed only at certain distinct material points traveling with the torch, such as T_x, T_y and T_z in Fig. 2, adjoining to the location of critical centerline cooling rate, maximum HAZ width and bead penetration, respectively.

Weld Pool

In the molten region, the experimental evidence (Refs. 31–35) in the general case suggests that in each half of the pool, the fluid motion of the melt consists of two flow streams with an opposite sense of circulation (*i.e.*, longitudinal vorticity — Fig. 3): the lateral stream 1, driven by surface tension and jet shear effects sideways and backward, to converge finally down, and the joint penetration stream 2, driven by external arc momentum downward and back, to diverge finally upward. Both streams originate at the fusion front of the pool or the surface distribution area of the externally added material, and eventually terminate at the solidification front at the back of the pool. As for the occasionally observed single-stream circulation in the melt, it can be considered as a degenerate case of the above formulation, in which one stream dominates and absorbs the other.

Also, the conservativeness of the thermal and flow fields in the pool requires that the weld geometry characteristics (width w, depth d, height h) be primarily dependent on the local temperature and velocity distribution, while remote thermal and flow conditions have an indirect effect through the local ones. Thus, the bead width is determined by the lumped, scalar characteristics (states) of the lateral stream 1, *i.e.*, its total mass m_1, average velocity v_1 and equivalent temperature T_1, while the penetration is defined by the respective states m_2, v_2, and T_2 of stream 2. These scalar quantities enter the local, lumped energy balances determining the rates of change of the pool width w and depth d, while the height h is computed through a mass balance of the molten reinforcement:

width w — local energy balance in y:

$$Q_{my}(w)=Q_{11}(v_1T_1)-Q_{sy}(T_y) \qquad (3)$$

depth d — local energy balance in z:

$$Q_{mz}(d)=Q_{12}(v_2,T_2)-Q_{sz}(T_z) \qquad (4)$$

height h — local mass balance of reinforcement :

$$m_r(m_1 + m_2, h) = m_e - m_{rx}(T_x) \tag{5}$$

where for the heat Q and mass m rates, the first subscript m = latent heat or mass fused, s = conducted heat to the solid, l = heat convected and conducted in the melt, e = external torch transfer, and the second subscript indicates direction or flow stream. For the two streams, the rates of change for their lumped states (m_i, v_i, T_i) are determined by one-dimensional balances of mass, momentum and energy, respectively as follows:

$$\text{mass balances (continuity):}\quad m_i = m_{mi}(w, d, h) + m_{ei} + m_{12} \tag{6}$$

$$\text{momentum balances (Navier–Stokes)}\quad J_i(v_i) = \sum F_{ki} + F_{ei} + J_{12} \tag{7}$$

$$\text{energy balances : } E_i(T_i) = -Q_{si}(T_x, T_y, T_z) - Q_{mi} - Q_{ai} + Q_{ei} + E_{12} \tag{8}$$

where m, J and E are the rates of change for mass, momentum and energy. These balances provide for heat transfer to the solid region and to the environment (subscript a), latent fusion-solidification effects (m), external transfer from the torch (e) and state exchange between the streams (12). In the Navier-Stokes equations, the partial equivalent forces ΣF_{ki} acting on each stream include the natural convection (buoyancy) forces, inert gas jet shear, surface tension (Marangoni), electromagnetic (Lorentz) and viscous friction forces to the solid interface. Analytical expressions for these terms are derived in Ref. 30.

Computational Integration and Experimental Calibration

The boundary conditions on the pool surface include heat, momentum and possibly mass transfer from the torch, when a consumable electrode is used (e.g., in GMAW). The distribution q(x,y) of these torch effects, as well as the terms in the balances above, are partitioned to the two streams according to the adjustable position r of the torch relative to the boundary surface between the streams — Fig. 3. This boundary is determined by the pool geometry (w,d,h) and the stream volumes (*i.e.*, m_1, m_2), and defines the partial efficiencies n_1, n_2 in Equation 1:

$$n_1(r) = n.erfc\left(\frac{r}{\sigma\sqrt{2}}\right), \quad n_2(r) = n - n_1(r) \tag{9}$$

where n and σ are the total efficiency and distribution radius of the torch. This distribution can be modified as necessary for eccentric locations of the torch, multiple sources, etc. The torch description is integrated to the solid conduction and pool flow model through an iterative computation algorithm, coded in a nonlinear dynamic simulation language and executed at real-time speed by ordinary microcomputer hardware, as follows:

1) For a given set of the source pair parameters (n_1, σ_1), (n_2, σ_2) in the solid area, the conduction field yields the heat fluxes Qs at the pool interface in the energy balance (Equations 3, 4, 8).

2) The balances of the molten pool (Equations 6–8) determine the states of the two streams and the weld bead geometry (Equations 3–5).

3) The temperatures T_y and T_z are determined by interpolation of the solidus isotherm T_m through locations w and d.

4) The composite conduction relationships (Equation 2) for temperatures T_y and T_z yield the partial efficiencies of the source pair (n_1, n_2).

5) The distribution radii σ_1, σ_2 of this pair are determined by off-line calibration experiments or real-time identification through measurement of T_x, T_y, and T_z.

This last iteration step requires experimental calibration of the torch parameters (n, σ_1, σ_2) of the model before its execution. These parameters are selected so that the model prediction of the weld bead geometry matches the experimental weld bead shape at the nominal operation point of the process. The experimental tests were carried out on a computer-controlled welding setup, consisting of a multiprocess CC/CV power source rated at 400 A, a roll feeder of ER70S-6 consumable wire (0.89 mm diameter), a water-cooled GMAW welding gun (400 A), an inert gas (Ar-2%O_2) supply at a flow rate of 23.6 L/min (11.1 ft^3/h), and a servo-driven x-y positioning table supporting the weldment. The tests consisted of bead-on-plate GMAW on orthogonal mild steel plates, 12.7 mm (0.5 in.) thick, in which the nominal conditions were defined at an arc voltage of 30 V, welding gun velocity of 6 mm/s (14.2 in./min) and wire feed rate of 254 mm/s (600 in./min). The resulting weld beads were sectioned, polished (600 grit), etched in a HCl-HNO_3 solution and pictured under magnification (3X). Thus in Fig. 1, the predicted bead cross-section of the model (dashed line) is fitted to the average weld bead profile along the experimental GMAW bead at the nominal conditions. The calibration can also be slightly readjusted to obtain a better match of the particular bead section of the figure by the model (solid line). Further information on the hybrid welding model is detailed in Ref. 30.

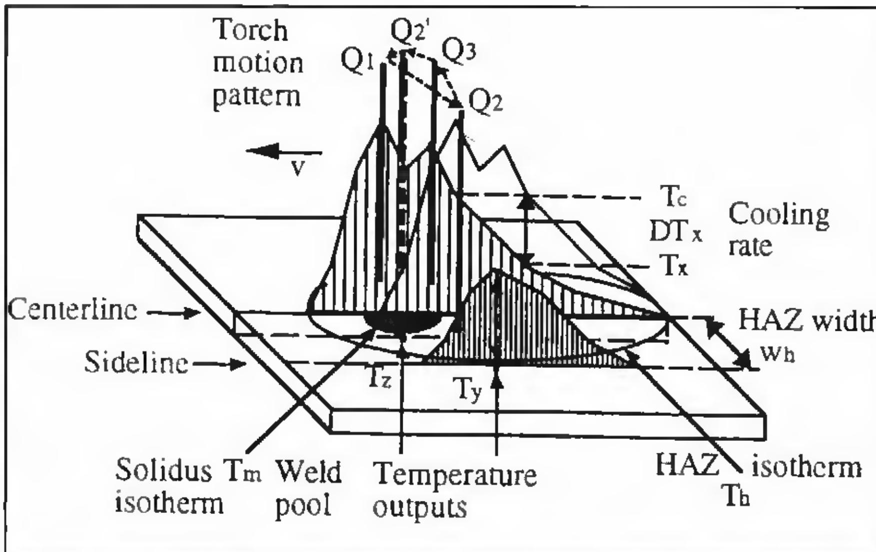

Fig. 4 — Heat inputs and temperature outputs of the time-shared welding gun configuration.

Multitorch Control of Material Structure

The dynamic thermal model of arc welding established above provides a reference basis for the design of control systems of the temperature field developed during the process. Since the eventual intention is to regulate the final microstructure and material properties of the weld, these features must first be associated with the predicted temperatures of the model — Fig. 4.

Solidification structures in the weld bead. The adverse effects of solidification faults on the mechanical properties of the joint must usually be collectively con-

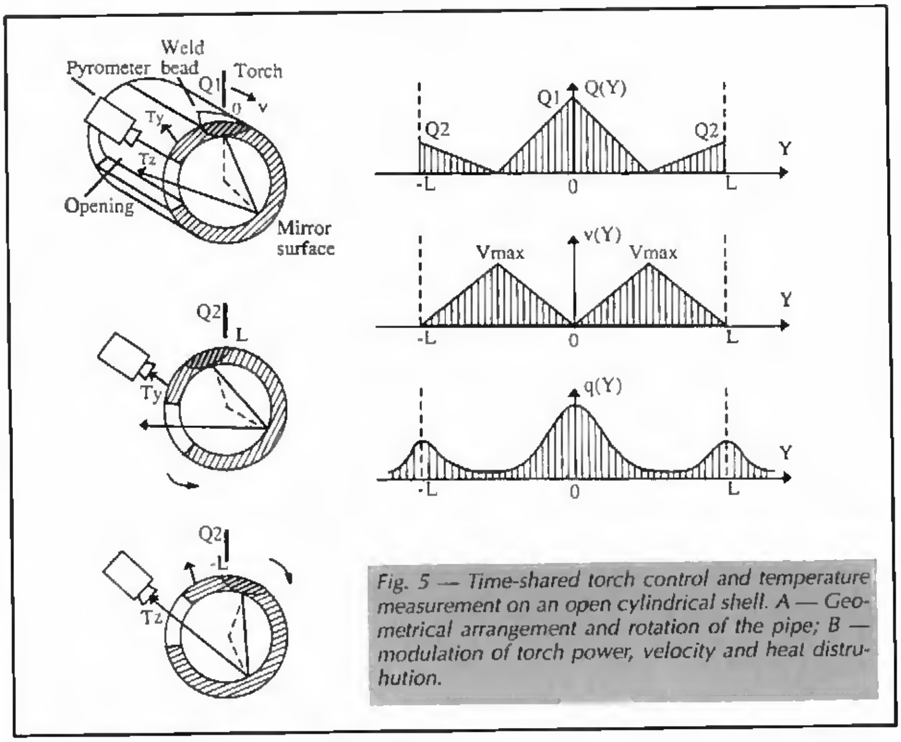

Fig. 5 — Time-shared torch control and temperature measurement on an open cylindrical shell. A — Geometrical arrangement and rotation of the pipe; B — modulation of torch power, velocity and heat distruhution.

trolled by minimizing the weld bead cross-section, without reducing the useful loaded joint area. To ensure full penetration of the joint, the bead depth d, which is difficult to sense in-process, must be controlled to cover the entire plate thickness D. Equivalently, the readily measurable maximum backbead temperature T_z must be regulated to a setpoint at least equal to the solidus temperature T_m.

Equilibrium structures in the heat-affected zone. The width of the HAZ isotherm T_h must be controlled within an allowed value w_h. Alternatively, the peak temperature T_y at distance w_h from the weld centerline can be regulated to temperature T_h. This method is preferable since T_y can be sensed by a single spot temperature measurement, and its dependence on the torch conditions is more nearly linear than that of w_h.

Nonequilibrium structures related to the cooling rate. The maximum cooling rate $\dot{T}_{cr}$ at a critical temperature T_c appears on a centerline location x. If the temperature of this material point is measured again and found to he T_x after one sampling period δ, the temperature drop:

$$\Delta T_x = T_c - T_x = \int_0^{\delta} \dot{T}_{cr}(\tau)\, d\tau \qquad (10)$$

gives an integrated, less noisy measure of the cooling rate (*i.e.*, $\dot{T}_{cr} = \partial T/\partial t \approx \Delta T_x/\delta$), and needs only a single subsequent spot temperature measurement T_x at point x and time δ.

Thus, the material structure can be controlled by the regulation of spot temperatures T_x, T_y, T_z (outputs) at carefully chosen locations, to specific temperature setpoints. However, Equation 2 indicates that the only general manipulatable process conditions (inputs) available for this purpose are the torch power Q and velocity v, and in certain processes the thermal distribution σ (e.g., through the arc length) and wire feed rate f of the consumable GMAW electrode. Except for the heat input Q, it can be seen in Equation 2 that the effect of the other torch conditions on the thermal field is clearly nonlinear. Moreover, in materials with multiple metallurgical transformations, the arc welding process does not provide a commensurate number of modulatable inputs to control the thermal outputs.

In the literature, multiple independent heat sources have been proposed to reshape the temperature field in analogous welding situations. In Ref. 36, a secondary torch following the primary one along the weld centerline was introduced to implement an in-process postheating cycle. In Ref. 37, a split-beam laser source was used for preheating, and in Ref. 38, two lateral oxyfuel torches were employed to mitigate residual stress and distortion effects. A similar multiple heat input arrangement for regulation of several microstructural welding outputs is shown in Fig. 4. Note that the torches are positioned so as to exert preferential (decoupled) thermal effects on certain temperature locations, which greatly improves the control system performance.

Since such multiheat source configurations introduce the cost and complexity of multiple independent power supplies, as well as potential interference among the arcs. A single heat source can be multiplexed in time (time-shared) between multiple heat input locations. This is done by a rapid repetitive cycling motion pattern of the arc on the weld surface, so as to mimic the effect of multiple torches. In Fig. 4, a coordinated reciprocation of the part in the y-direction and of the torch in the x-direction, together with a modulation of its power Q can implement the action of the individual torches and provide the heat inputs Q_1, Q_2, Q_3 needed for decoupled regulation

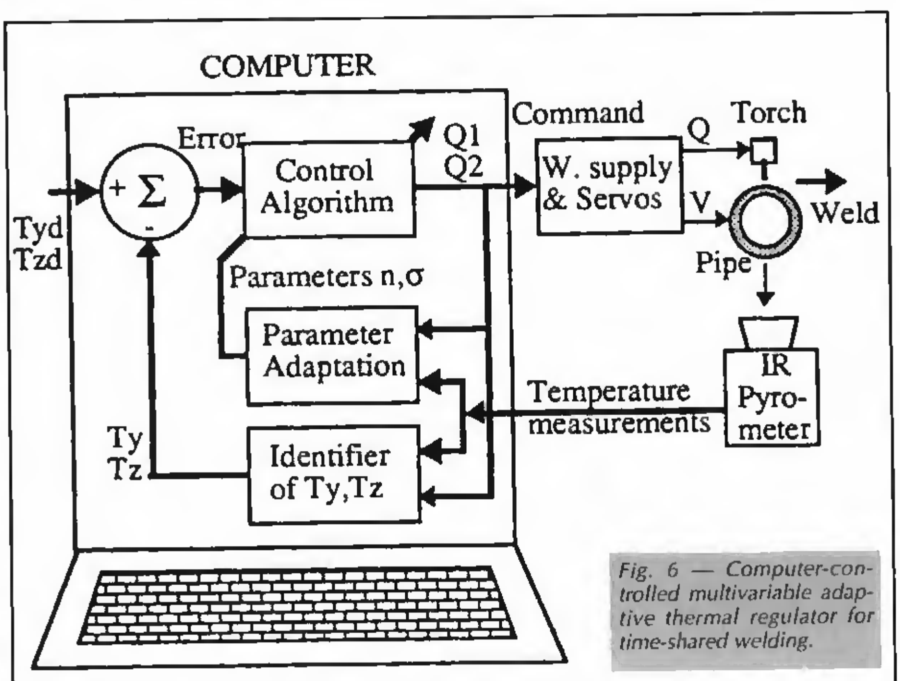

Fig. 6 — Computer-controlled multivariable adaptive thermal regulator for time-shared welding.

of the output temperatures T_x, T_y, T_z. These can be measured periodically in-process by a noncontact infrared pyrometer and used as thermal feedback to the microstructure controller system.

Experimental Implementation

This time-shared multitorch configuration for material structure control is applied to longitudinal gas tungsten arc welding (GTAW) of open cylindrical shells — Fig. 5. The same laboratory setup was used as for the calibration experiments above, with the GMA welding gun/wire feeder replaced by an air-cooled GTAW torch (300 A). The experiments consisted of bead-on-plate longitudinal welding of a stainless steel (304) slotted pipe, with diameter of 50.8 mm (2 in.) and a thickness D = 3.125 mm (0.12 in.). The torch voltage was V = 12 V, the longitudinal velocity v = 2 mm/s (4.7 in./min), and the inert gas flow rate 0.4 L/s (0.2 ft^3/h). For this stainless steel, the weld bead section must be controlled through the backbead temperature T_z to avoid an extensive columnar solidification structure, dilution of the bead composition due to segregation in undesirable phase areas of the Maurer diagram, and possible oxidation of regions not reachable by the inert gas flow (*e.g.*, back bead). The HAZ must also be regulated via the peak temperature T_y to avoid sensitization, *i.e.*, formation of Cr_4C at the grain boundaries and depletion of the adjacent areas from Cr, as well as secondary nucleation of brittle σ-phase. Regarding cooling rate related phenomena, thermal cracking is usually not critical and thus control of the centerline temperature drop ΔT_x need not be implemented. Thus, the temperatures T_y and T_z must be regulated to set points related to the HAZ T_h and solidus T_m isotherms, respectively, and selected as T_{yd} = 1260°C (2300°F) at w_h = 5 mm, and T_{zd} = 1241°C (2266°F). The necessary lumped heat inputs Q_1 and Q_2 are time-multiplexed by modulating both the single GTAW torch power Q and velocity v as a function of its transverse position Y relative to the part, thus yielding a continuous circumferential heat distribution q on the (x,y) plane — Fig. 5:

$$q(x,y)=\int_0^L \frac{n.Q(Y)}{v(Y)\tau.2\pi\sigma^2} \exp\left(-\frac{x^2+(y-Y)^2}{2\sigma^2}\right)dY \tag{11}$$

where L = ±3 mm is the distance and τ = 0.25 s the transition time between Q_1 and Q_2. The modulated rotation of the part needed to implement the double-torch arrangement is undertaken by a servo-driven rotor stage (LPS 214) mounted on the x-y positioning table of the setup. This cyclic motion of the part also enables the periodic measurement of the temperatures T_y and T_z, respectively, on the external and internal surface of the weld (observed by its reflection on the opposite surface through the pipe slot), by a single-spot infrared pyrometer (OS 441) every δ = 1 s. A standard microcomputer system handles the thermal data acquisition from the pyrometer by an internal multipurpose input/output board (NI-Lab NB), as well as the actuation of the rotor servo-system and the multiprocess power supply, as shown in Fig. 6.

The thermal control system, implemented by the computer software is designed on the basis of the composite model developed above, with the double-torch heat distribution (Equation 11) in place of Equation 9. The linearized dependence of the individually manipulated heat inputs Q_1, Q_2 on the temperature outputs T_y, T_z is assessed by small perturbation (sensitivity) analysis of this model, and as suggested by Equation 2, it can be expressed in the form of ordinary differential equations (ODEs):

$$\tau_{ij}\dot{y}_i(t)+y_i(t)=K_{ij}u_j(t)$$
$$\text{where } y_i(t)=T_y,\ T_z$$
$$\text{and } u_j(t)=Q_1,\ Q_2 \tag{12}$$

where K_{ij} and τ_{ij} are the gains and time constants of the first-order transfer functions. These dynamic parameters, which depend on the joint geometry and material, the initial temperature and boundary thermal conditions, as well as the process variables, can be identified in the neighborhood of the nominal welding conditions from computational and experimental step response tests (Ref. 30), and are collected in Table 3.

Note that the small values of the gain K_{z2} relative to K_{y2} indicate a rather weak influence of the heat input Q_2 on the bead penetration, and its decoupled effect on the HAZ width, as expected. The variation ranges of the dynamic parameters in Table 3 for test steps of various sizes in the heat inputs Q_1 and Q_2, are attributed to the welding process nonlinearity, as described by the model. Moreover, the thermal drift of the material properties, as the workpiece is heated during welding, results in a nonstationary (time-varying) process. Additionally, the variation ranges of Table 3 reflect several disturbances of the welding geometry, environmental conditions and process characteristics, such as changes of the torch efficiency or distribution. This modeling uncertainty requires real-time identification of the dynamic parameters, as well as in-process adaptation of the control unit to the adjustments of the model. The feedback control system adopted in Fig. 6 is based on a multivariable adaptive algorithm (Refs. 39, 40) employing continuous measurement of the heat inputs and temperature outputs, to estimate the welding parameters and update the reference model of the controller, that modulates the double-torch heat distribution. Thus, the material structure and properties of the weld are regulated through the temperature field

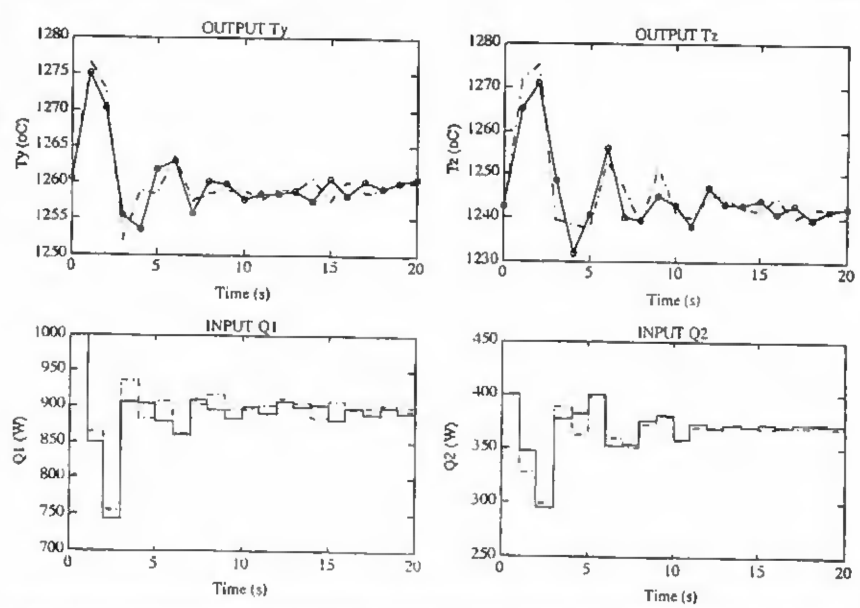

Fig. 7 — Time responses of the temperature outputs T_y, T_z and heat inputs Q_1, Q_2 of the thermal regulator, after a step change of the preheat to T_o = 100°C at t = 0. (o-o: experimental tests, -.-.-: model simulations).

Table 3 — Experimental Dynamic Parameters of the Linearized GTAW System Model

Input	Nominal value	Test Range	Temperature T_y K_{yi}	Temperature T_y τ_{yi}	Temperature T_z K_{zi}	Temperature T_z τ_{zi}
Q1	1000 W	800–1200 W	0.63–0.71	3.6–4.1	0.72–0.81	2.5–3.1
Q2	400 W	320–480 W	1.20–1.42	1.4–2.1	0.18–0.23	4.7–5.4

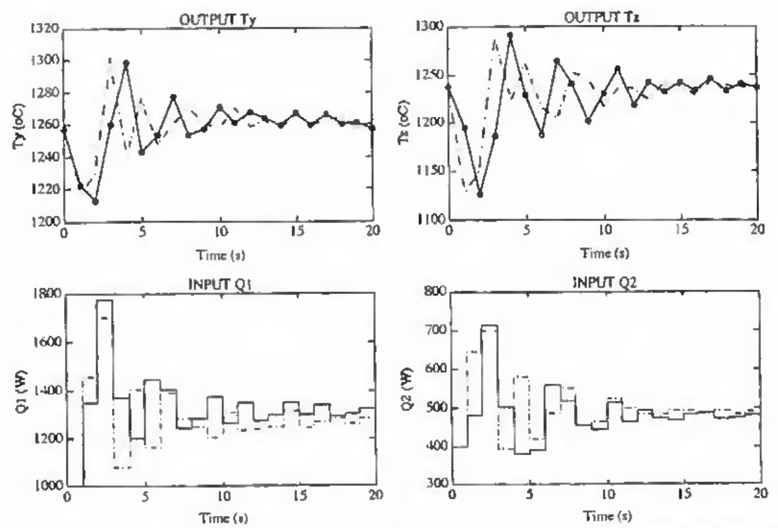

Fig. 8 — Time responses of the temperature outputs T_y, T_z and heat inputs Q_1, Q_2 of the thermal regulator, after a step change of the torch speed to v = 3 mm/s at t = 0. (o-o: experimental tests, -.-.-: model simulations).

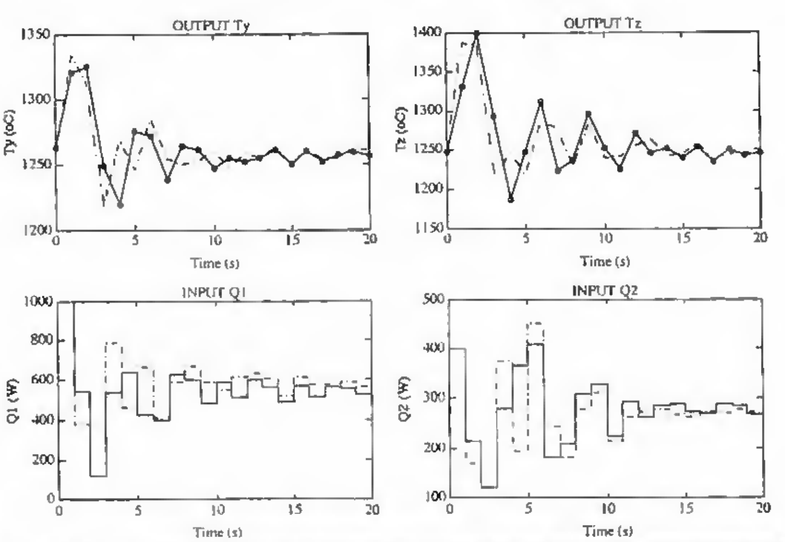

Fig. 9 — Time responses of the temperature outputs T_y, T_z and heat inputs Q_1, Q_2 of the thermal regulator, after a step change of the wall thickness to D' = 2 mm at t = 0. (o-o: experimental tests, -.-.-: model simulations).

to the desired setpoints (T_{yd},T_{zd}) despite the presence of process disturbances.

The performance of this welding control system was tested by experiment and by simulation in rejecting geometrical, thermal and process condition disturbances. Figure 7 shows the time responses of the temperature outputs T_y, T_z and heat inputs Q_1, Q_2 when the torch at t = 0 crosses the boundary between two mechanically connected, but thermally insulated sections of the pipe, with the second section preheated to about T_o = 100°C by previous welding. Figure 8 illustrates a similar behavior of the system inputs and outputs, when the longitudinal speed of the torch v is suddenly increased to v = 3 mm/s at t = 0. Last, Fig. 9 presents analogous thermal transients when the torch encounters at t = 0 a step reduction of the wall thickness to D' = 2 mm, milled on the inside surface of the pipe — Fig. 10. In all three cases, and despite the initial deviations of the temperatures T_y and T_z from the desired setpoints T_{yd} and T_{zd}, especially after the geometrical and torch velocity disturbance, the thermal and thus, the microstructural outputs are eventually restored to the nominal values and the effects of the disturbances are completely rejected. The duration of the transients is currently limited by the speed of the time-shared welding arrangement and the infrared sensor. Also, the simulated model responses match well the experimental transients, although the deviations between the steady-state values of the heat inputs necessary for rejecting the disturbances, indicate minor static modeling imperfections. Despite these effects, the thermal regulation objective is satisfied in all cases.

Conclusion

In the previous discussion, it has been explained that simultaneous thermal control of multiple material structures and properties of the weld require multiple-source configurations, implemented by a single time-multiplexed heat source, and arranged so as to exert decoupled influences on the weld features. However, such an arrangement of a finite number of localized heat inputs allows independent regulation of an equal number of thermal outputs, in limited ranges of specified set-points (Ref. 40). To relax this restriction and to maximize the control authority over the entire distributed microstructure field of the weld, the time-shared torch idea is generalized to a continuous heat distribution on the full accessible part surface, with independently modulated intensity at each individual location. Also, temperature mea-

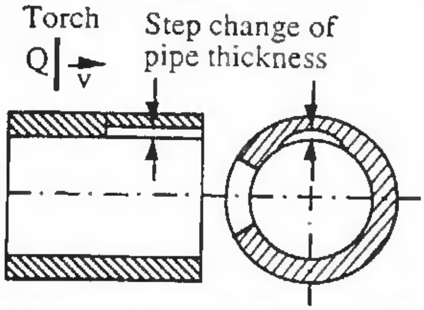

Fig. 10 — Step geometrical disturbance.

surements on the entire weld surface are needed for in-process estimation of the internal material structure and properties. Thus, a distributed-parameter formulation must be adopted for process modeling and closed-loop control of the material structure and property distribution in the weld.

Figure 11 illustrates this distributed welding technique in peripheral GTA welding of thick cylindrical shells and pipes. The heat input distribution on the weld surface is implemented by continuous fast rotation of the part and by coordinated transverse (*i.e.*, axial) motion of the torch and the pyrometer by separate translational servo-systems. This modulated deflection of the arc provides a rapid scanning motion pattern along circumferential trajectories (X(t),Y(t)) at various offsets Y(X) from the weld centerline, while a synchronized modulation of the torch power Q(t) yields the desired heat distribution q(X, Y, t). The infrared sensor also scans the temperature field T(x, y, t) across the external and internal surface, on the full or through the hollow alternating segments 1 and 2 of the test pipe. A thermal control system to regulate the topside $T_y(x)$ and bottomside Tz(x) temperature profiles, by modulating the arc power Q(X) and path Y(X), is currently under construction, based on a distributed version of the process model.

In summary, this research represents one stage toward the codification and automation of the experience and skills of the ancient smiths and modern welders, in obtaining sound material structures and properties in weld joints. Thermal modeling of these features, through a real-time, lumped dynamic description of the welding temperature field, and their adaptive feedback control through in-process thermal sensing and a time-shared multi-torch welding configuration, represent the major steps to this goal. This approach ensures real-time identification and in-process regulation of the welding process, despite the presence of unexpected disturbances in the weld geometry, thermal effects and process conditions. The technique is directly applicable to various weld arrangements (flat, cylindrical), part materials (mild and stainless steels) and welding methods with or without material transfer (GMAW, GTAW). In all these industrially important applications, the benefits of in-process microstructure control on the static and dynamic strength of the joint, fracture toughness, corrosion and oxidation resistance, as well as optimization of other related weld quality and productivity measures, are currently under experimental investigation.

Acknowledgment

This research was supported by NSF Grant DDM-9209141.

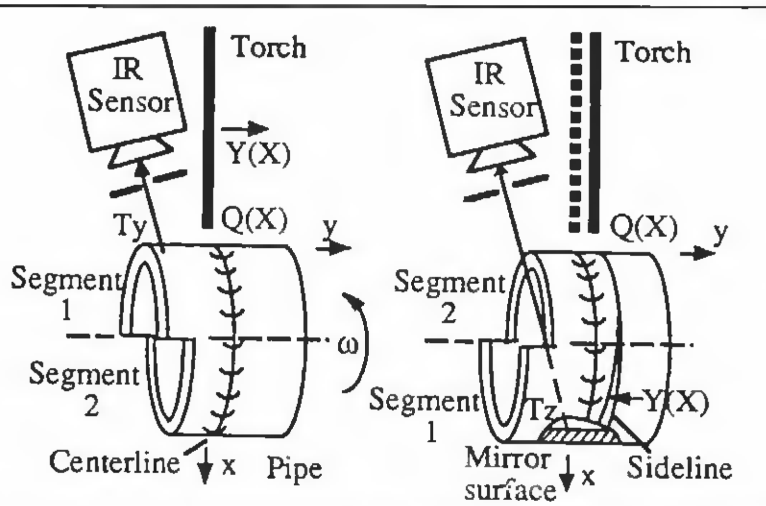

Fig. 11 — Scanned torch control and temperature measurement in girth pipe welding.

References

1. Latimor R. 1981. *The Iliad of Homer.* Vol. 18, pp. 468–482 and 608–614.
2. Udin, H., Funk, E. R., and Wulff, J. 1967. *Welding for Engineers.* Wiley, New York, N.Y.
3. Masubuchi, K. 1980. *Analysis of Design and Fabrication of Welded Structures.* Pergamon Press, New York, N.Y.
4. McClintock, F. A., and Argon, A. S. 1966. *Mechanical Behavior of Materials.* Addison-Wesley, Reading, Mass.
5. Brophy, J. H., Rose, R. M., and Wulff, J. 1964. The structure and properties of materials. Vol. II, *Thermodynamics of Structure*, Wiley, New York, N.Y.
6. Hayden, H. W., Moffatt, W. G., and Wulff, J. 1965. The structure and properties of materials. Vol. III, *Mechanical Behavior*, Wiley, New York, N.Y.
7. Linnert, G. E., *et al.* 1968. *Arc Welding.* Metals Engineering Institute, ASM International, Materials Park, Ohio.
8. Miyachi, H. 1989. In-process control of root-gap changes during butt welding. Ph.D. Thesis. Dept. of Mechanical Engineering, MIT, Cambridge, Mass.
9. Doumanidis, C. C., and Hardt, D. E. 1990. Simultaneous in-process control of heat-affected zone and cooling rate during arc welding. *Welding Journal* 69 (5): 186-s to 196-s.
10. Einerson, C. J., Smartt, H. B., Johnson, J. A., Light, D., and Moore, K. L. 1992. Development of an intelligent system for cooling rate and fill control in GMAW. *Third ASM Intl. Conf. on Trends in Welding Research*, Gatlinburg, Tenn.
11. Roberts. O. F. T. 1923. *Proc. Roy. Soc.* (A), pp. 104–640.
12. Rosenthal, D., and Schmerber, R. 1938. Thermal study of arc welding — experimental verification of theoretical formulas. *Welding Journal* 17(4): 2–8.
13. Rosenthal, D. 1941. Mathematical theory of heat distribution during welding and cutting. *Welding Journal* 20(5): 220-s to 234-s.
14. Rykalin, N. N. 1971. *The Calculation of Thermal Processes in Welding.* Mashgiz, Moscow.
15. Wells, A. A. 1952. Heat flow in welding. *Welding Journal* 31(5): 263-s to 267-s.
16. Roberts, D.-K., and Wells, A. A. 1954. A mathematical examination of the effect of bounding planes on the temperature distribution due to welding. *Brit. Welding J.* 1, pp. 553–560.
17. Grosh, R. J., and Trabant, E. A. 1956. Arc welding temperatures. *Welding Journal* 35(8): 396-s to 400-s.
18. Carslaw, H. S, and Jaeger, J. C. 1959. *Conduction of Heat in Solids.* 2nd ed., Oxford Press, London.
19. Adams, C. M. 1958. Cooling rates and peak temperatures in fusion welding. *Welding Journal* 37 (5): 210-s to 215-s.
20. Jhaveri, P., Moffatt, W. G., and Adams, C. M. 1962. The effect of plate thickness and radiation on heat flow in welding and cutting. *Welding Journal* 41 (1): 12-s to 16-s.
21. Barry, J. M., Paley, Z., Adams, C. M. 1963. Heat conduction from moving arcs in welding. *Welding Journal* 42: 97-s to 104-s.
22. Myers, P. S., Uyehara, O. A., and Borman, G. L. 1967. Fundamentals of heat flow

in welding. *Weld. Res. Council Bulletin* 123.

23. Kazimirov, A. A., Nedoseka, A. Y., and Sanchenko, V. A. 1973. Calculating the distribution of heat during butt welding of plates. *Autom. Weld. USSR* 26(11): 30 to 32 .

24. Kopersak, N. I., Slivinskii, A. M., and Dukhno, V. M. 1973. Temperature conditions in weld pools. *Autom. Weld. USSR* 7: 1 to 3.

25. Malmuth, N. D., Hall, W. F., Davis, B. I., and Rosen, C. D. 1974. Transient thermal phenomena and weld geometry in GTA welding. *Welding Journal* 53: 388-s to 400-s.

26. Nedoseka, A. Y., Sanchenko, V. A., and Vorona, G. A. 1977. Distribution of temperature when a concentrated source of heat acts on the surface of a plate. *Autom. Weld. USSR* 30(6): 1–4.

27. Nunes, A. C. 1983. An extended rosenthal model. *Welding Journal*, 62(6): 165-s to 170-s.

28. Willgoss, R. A. 1984. Mathematical model predicts equilibrium. *Weld. Met. Fab.* 52(9): 340–351.

29. Tsai, C. L. 1988. Modeling of thermal behaviors of metals during welding. *Trends in Welding Research in the U.S.*, pp. 77–89, ASM International, Materials Park, Ohio.

30. Doumanidis, C. C. 1992. GMA weld bead geometry: a lumped dynamic model. *International Trends in Welding Science and Technology*, pp. 63–67, eds. S. A. David and J. M. Vitek, ASM International, Materials Park, Ohio.

31. Bradstreet, B. J. 1968. Effect of surface tension and metal flow on weld bead formation. *Welding Journal* 47(7): 314-s to 322-s.

32. Woods, R. A., and Milner, D. R. 1971. Motion in the weld pool in arc welding. *Welding Journal* 50(4): 163-s to 173-s.

33. Bukarov, V. A., Ishchenko, Y. S., and Loshakova, V. G. 1978. The effect of convection of metal in the weld pool penetration. *Svar. Proiz.* (11): 4–7.

34. Mills, G. S. 1979. Fundamental mechanisms of penetration in GTA welding. *Welding Journal* 59(1): 21-s to 24-s.

35. Heiple, C. R., and Roper, J. R. 1982. Mechanism for minor element effect on GTA fusion zone geometry. *Welding Journal* 61(4): 97-s to 102-s.

36. Doumanidis, C. C., and Hardt, D. E. 1989. A model for in-process control of thermal properties during welding. *ASME J. of Dyn. Syst, Meas. & Control* 111: 40 to 50

37. Liu, Y. N., and Kannatey-Asibu, E., Dual beam laser welding. *Japan-U.S.A.Symposium on Flexible Automation* Vol. 1, ASME. pp. 283–290.

38. Miyachi, H. 1989. In-process control of root-gap changes during butt welding. Ph.D. thesis, Dept. of Mechanical Engineering, MIT, Cambridge, Mass.

39. Goodwin, G. C., Ramadge, P. J., and Caines, P. E. 1980. Discrete-time multivariable adaptive control. *IEEE Trans. on Aut. Control* Vol AC-25(3): 449–456.

40. Doumanidis, C. C., and Hardt, D. E. 1991. Multivariable adaptive control of thermal properties during welding. *ASME J. of Dyn. Syst, Meas. & Control* 113: 82–92.